A Method for Evaluating Contact Points with the SCOUT-Rover-Rimless-Wheels

[1]Jentsch, J., [1]Merker, L., [2]*Schütt, M., [3]Bock, A. S., [2]Lichtenheldt, R. & [1]Zentner, L.

*lead presenter, manuel.schuett@dlr.de

[1] Mechanics of Compliant Systems Group, TU Ilmenau, Germany

[2] Institute of System Dynamics and Control, German Aerospace Center (DLR), Germany

[3] Institute of Mathematics, TU Ilmenau, Germany

***Abstract* – Efficient locomotion in unpredictable and unstructured environments is a major challenge in mobile robotics, especially in planetary exploration. Scouting lava tubes on Mars or on the Moon is the primary mission of the Space Cave explOration UniT (SCOUT), developed at the Robotics and Mechatronics Center of the German Aerospace Center. The SCOUT is equipped with six rimless wheels combining the conventional locomotion capabilities of legged and wheeled robots. A major challenge for efficient locomotion on challenging terrain is the reliable detection and localization of contacts between each rimless wheel and the ground. This work shows that it is possible to implement ground contact detection for rimless wheels without installing additional sensors by relying solely on the motor currents. We present an algorithm based on experimental data recorded with the SCOUT. Beyond contact detection, the presented approach allows the inference of additional angular information of the respective foot contacting the ground and, subsequently, the contact position with respect to the rover's body frame. The contact detection approach has promising implications for the operational performance and energy efficiency of the SCOUT.**

I. Introduction

Within the last six decades, planetary exploration using rovers has been a crucial driver of scientific and technological advancement. However, navigating unstructured environments with unpredictable terrain and extreme conditions remains a significant challenge in mobile robotics. Traditional wheeled rovers excel in providing smooth mobility on structured and even surfaces typically found in industrial settings. However, in the unstructured and obstructed terrains typical for space exploration, conventional wheels face significant limitations. For instance, well-known wheeled rovers such as *Opportunity*, *Spirit*, and *Curiosity* developed by NASA have successfully traversed the surface of Mars but only at selected locations with few obstacles [1]. Legged robots such as *SPOT* and *ATLAS* developed by *Boston Dynamics*® have successfully tackled the challenge of traversing rough terrain [2,3], but they are not yet specialized for space applications. Another approach to traverse rough terrain is exploiting rovers with tank-like tracks [4]. However, tracks tend to accumulate soil material, which, at worst, can block the driving appendages.

In response to the need for versatile mobility solutions, researchers have explored innovative hybrid designs such as *wheel-legs*, also known as *whegs* or *rimless wheels* [5]. These designs aim to integrate the benefits of both walking and rolling capabilities. A pioneering example in this field is the *RHex*, which has demonstrated the ability to navigate rough terrain and climb stairs higher than the radius of its whegs [6]. This rover uses a special type of rimless wheel,

consisting of a single C-shaped spoke. The chassis of the rover is essentially a rigid body with limited adaptability to varying terrains. Other approaches exploit rimless wheels including multiple legs, such as the *Cyote III*, *Rowdy Runner II* or rovers using *DAGSI* whegs [7-9]. The Cyote III was designed for space exploration. It consists of two segments and four rimless wheels, each including five compliant pre-curved legs [10]. The Rowdy Runner II uses two rimless wheels with seven straight spokes, serving as radially protruding spring/damping elements. The DAGSI whegs do not provide any suspension to the rover. Instead, the design objective is to optimize the climbing characteristics of the spoke surface.

This paper focuses on the Space Cave explOration UniT (*SCOUT*), which utilizes a special design featuring six rimless wheels and flexible backbones allowing it to adapt to the environment in various gaits [11], see Fig. 1. Each rimless wheel consists of a rigid wheel hub with three C-shaped compliant spokes, arranged at 120° intervals, and featuring rounded compliant feet at the ends. To extend maneuverability, all wheels are actuated by individual motors. The main mission of the SCOUT is to explore volcanic formations known as lava tubes on Mars or on the Moon. These tubes are remnants of past volcanic activity and promise to offer stable temperatures and radiation levels. As these conditions increase chances of discovering traces of microbial life, they are of particular interest for planetary exploration. The SCOUT aims to drop down into these tubes through collapsed segments (skylights) and to autonomously explore the internal cave structures. Due to unpredictable obstacles, ground conditions and limited optical sensors during cave exploration, tactile environmental awareness is a crucial aspect contributing to the SCOUT's main mission. The present paper addresses this issue with the aim of realizing a simple mechanism for the detection and localization of rimless-wheel-ground-contacts. Naturally, localizing contact points between each leg of the rimless wheel and the ground might be realized using additional tactile sensors distributed along the legs, but also using various sensors located at the wheel hub. For instance, it has been shown that contact points between slender compliant structures, such as the legs of a rimless wheel, and the environment can be effectively determined based on angular, force and torque information [12-14]. However, in context of the SCOUT, each additional sensor represents a single point of failure impairing the rover’s robustness. Therefore, our objective is to dispense with additional sensors using the motor current signals for contact detection and localization, thereby integrating multiple functions into the components already installed.

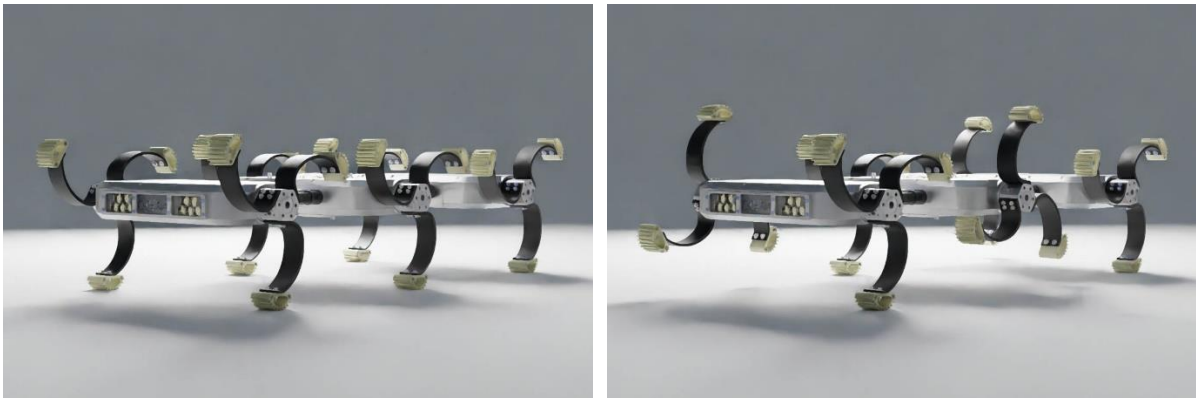

(a) Wheel configuration for the synchronous wheel *(b) Wheel configuration for the tripod wheel*

Fig. 1 Comparison of wheel configurations for different gaits

This paper proposes a novel reliable method for estimating ground contacts with the SCOUT's rimless wheels based on motor currents. The noisy current signals are analyzed and compared

to theoretical signal sequences resulting from a rigid rimless wheel walking model, allowing a simplified but reliable contact estimation based on a purely geometric approach. Furthermore, angular contact localization is integrated to support various rover gaits, which influence performance and operational scenarios.

II. Methods

This section describes the experimental test cases with the SCOUT in Section II A, which were performed to provide a database. In Section II B, analytical modelling equations are derived for further analysis of the database in Section II C.

A. Experiments

For the hardware experiments, the SCOUT was used to realize three primary cases [15]:

1) *Free-Wheel (FW) Case*: The wheels are free to rotate unobstructed (no contacts);
2) *Synchronous-Wheel (SW) Case*: All wheels are driven in unison, see Fig. 1(a);
3) *Tripod-Wheel (TW) Case*: Three wheels are synchronously driven, and the remaining three wheels have a 60° phase shift, with the phase shift occurring between opposing wheels, see Fig. 1(b).

Fig. 2 SCOUT setup during FW case

All cases were executed with a target angular velocity of 3.14 rad/s and a minimum of five wheel-revolutions. The SW and TW cases were performed on rigid level ground. For the FW case, the rover was jacked up to ensure that all wheels could turn freely, see Fig. 2.

B. Simplified Modeling Approach

We consider a single rimless wheel according to Fig. 1 in contact with level ground, coming up with the plane, quasi-static, rigid model in Fig. 3. The wheel hub is represented by a circle of radius R and the foot elements by circles of radius r with radial distances l from the wheel center.

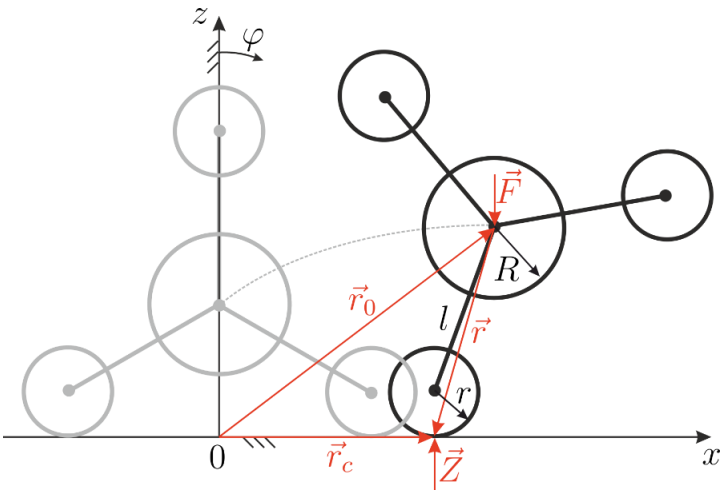

Fig. 3 Geometric representation of the rimless wheel

First, we consider the case $\varphi \in (0°, 120°)$ with a single foot in contact with the ground, assuming an ideal rolling like behavior. The basic geometrical relationships from Fig. 3 are represented by equations (1-3):

$$\vec{r}(\varphi) = -\left[l \sin\left(\varphi - \frac{\pi}{3}\right)\vec{e}_x + \left(l \cos\left(\varphi - \frac{\pi}{3}\right) + r\right)\vec{e}_z\right] \tag{1}$$

$$\vec{r}_c(\varphi) = \left(r\varphi + l \sin\left(\frac{\pi}{3}\right)\right)\vec{e}_x \tag{2}$$

$$\vec{r}_0(\varphi) = \vec{r}_c(\varphi) - \vec{r}(\varphi) \tag{3}$$

If we assume any force $\vec{F} = -F\vec{e}_z$ acting at the center of the wheel, the equilibrium conditions yield:

$$\vec{F} = \vec{Z}, \quad \vec{M}(\varphi) = \vec{r}(\varphi) \times \vec{F} \tag{4}$$

However, for a full revolution of the rimless wheel, its 120° symmetry results in a 120° periodic contact transition from one leg to another. Hence, it can be shown that the motor torques resulting from the SW and TW cases for arbitrary angles φ can be expressed similarly to [16] using (4) and a 120° periodic angle $\varphi_p(\varphi) = \mathrm{mod}\left(\varphi, \frac{2}{3}\pi\right)$:

$$M_{SW}(\varphi) = \left(\vec{r}\left(\varphi_p(\varphi)\right) \times \vec{F}\right)\vec{e}_y \tag{5}$$

$$M_{TW}(\varphi) = \begin{cases} M_{\mathrm{FW}}(\varphi) = 0, \text{if } \varphi \in \frac{\pi}{6}[4n-1, 4n+1], & n \in \mathbb{N}^0 \\ 2 \cdot M_{\mathrm{SW}}(\varphi) \quad \text{, else} \end{cases} \tag{6}$$

In (6), the factor of 2 emerges as a consequence of the distribution of the force $\vec{F}$ in the SW case, which is apportioned to two opposing (synchronous) wheels, whereas in the TW case, it alternately acts on only one of the opposing wheels. Given the complexity of modeling electromagnetic effects in combination with friction effects and the aim of maintaining a simple model, it is postulated that $M_{\mathrm{FW}} = 0$, thereby also disregarding inertial effects. In addition, neglecting frictional effects, we assume that the motor currents are proportional to the motor torques (5) and (6), where k is an unknown proportional factor:

$$I_i(\varphi) = k \cdot M_i(\varphi), i \in \{\mathrm{SW}, \mathrm{TW}\} \tag{7}$$

C. Data analysis approach

Figure 4 shows the ideal motor torques according to (5) and (6) with an exemplary force $|F| = 27\text{N}$ (estimated gravitational force acting on each SW) and true dimensions of the wheels. This serves as a basis for later comparison of real data with these ideal torques.

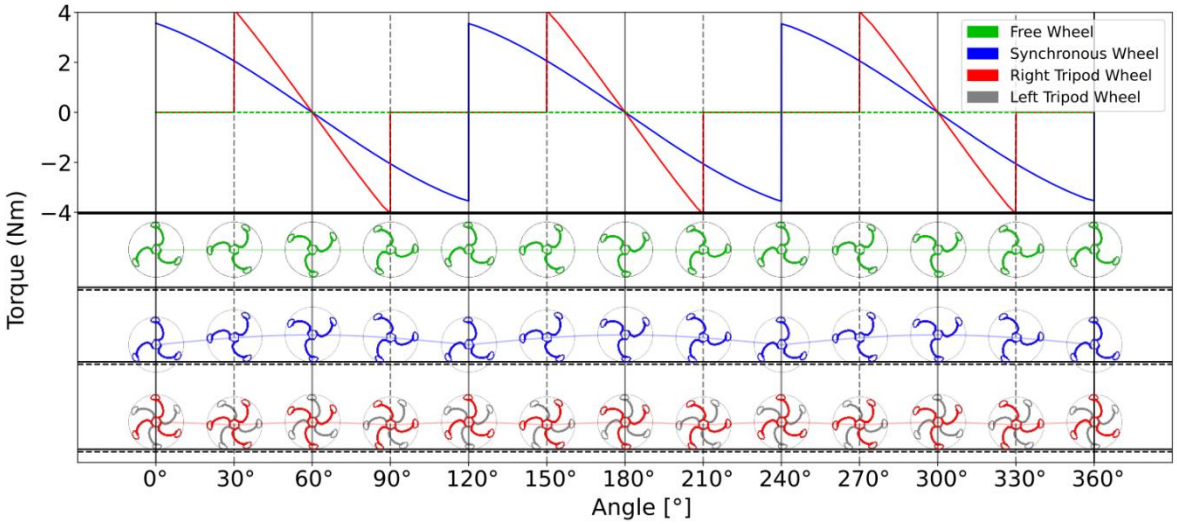

Fig. 4 Torques for the ideal FW-, SW- and TW-case for an entire wheel revolution

For a simplified understanding of the motor currents, the corresponding gaits (SW or TW) and the FW case are outlined for characteristic rotation angles φ. In the SW case (blue), the 120° periodic contact transition from one leg to another of the rolling rimless wheel results in jumps of the motor torque from its minimum to its maximum value. In the TW case, the considered rimless wheel is the right wheel, which is indicated in red, whereas the opposed (left) wheel is shaded in gray. Importantly, the left wheel affects the motor torque of the right wheel, as it repeatedly lifts the rover chassis, resulting in the right wheel spinning temporarily free (FW case). For clarity, Fig. 1(b) of the tripod gait can be compared to the initial position of the graph shown in Fig. 4. A contact variable $C(\text{t})$ is introduced, which is 0 (no ground contact) or 1 (at least one of the legs is in contact). Ideally, in the SW case, $C(t) \equiv 1$, whereas in the TW case $C(t) \equiv 1$, if $M_{\text{TW}} \neq 0$, see Fig. 5. Contacts are indicated by colored bars, where each color represents the respective leg in contact. The FW case, as part of the TW case, corresponds to $C(t) \equiv 0$, see (6). Importantly, walking on level ground, all currents are characterized by a 120° periodicity.

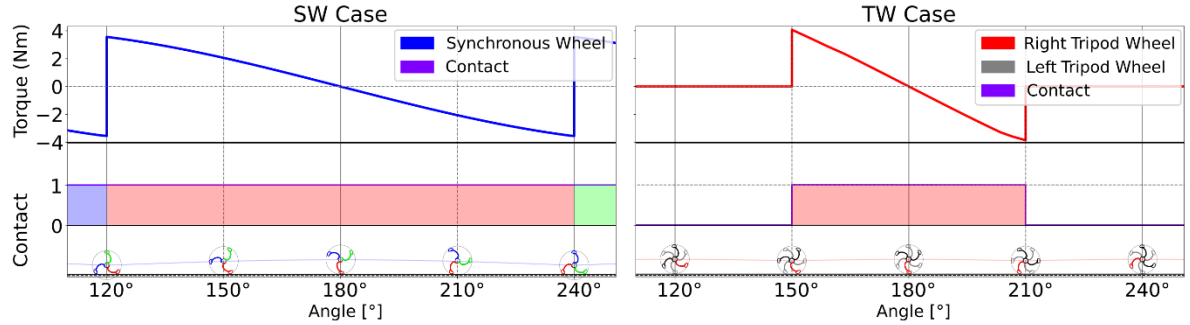

Fig. 5 Ideal contact behavior: SW case (left); TW case (right)

Naturally, in contrast to the data in Fig. 5, the measured data is affected by dynamic effects, the compliance of the rimless wheels and the overall system, as well as significant noise. However, if operated on ideal level ground, these aspects do not affect the 120° periodicity of the

measured motor torques and currents. Therefore, in the absence of any unevenness, the 120° periodicity applies for both the ideal and the measured motor torques and currents. As for the theoretically generated ideal data, the contact intervals are known by the geometry of the rigid rimless wheel, see Fig. 5. The proposed contact estimation is based on a phase tuning approach, optimizing the phase coherence between the measured motor controller data and the ideal reference courses from Fig. 4. Once phase coherency is achieved, the contact intervals resulting from the real measurement can be approximated using the ideal data from Fig. 5. In this way, the recorded motor controller data described in Subsection B is evaluated and compared to the ideal reference courses from Fig. 4, using the following procedure:

1) The noisy motor currents are post-processed based on a Fast Fourier Transformation (FFT) analysis using a band-stop filter with a rejection interval of 20-30 Hz to eliminate disturbing frequencies. In addition, a Savitzky-Golay filter with a window width of 61 samples and a polynomial order of 5 was applied to reduce data noise.
2) The proportional factor k in (7) is determined based on the mean value of the maximum motor currents. Note that this step is not necessary for the actual phase tuning approach, but solely for a simplified comparison of the ideal and measured data in Figs. 6 and 7.
3) The entire (filtered) motor current signal is divided into 120° subintervals.
4) For each subinterval q, the local phase shift φ_q w.r.t. the ideal data is determined using convolution for local phase tuning.
5) The mean $\bar{\varphi}$ and standard deviation s_φ of all local phase shifts φ_q are computed.

Finally, the filtered and phase tuned data is assumed to match with the contact intervals in Fig. 4, resulting in an approximation of the contact position. In addition, the parameters $\bar{\varphi}$ and s_φ are assumed to include information about the unevenness of the ground and, by comparison of the mean deviation of the local phase shift φ_q with the standard deviation s_φ, to potentially reveal information of overridden obstacles.

III. Results and Discussion

Figure 6 shows an exemplary 120° interval of the measured motor currents resulting from the SW case and the TW case, which are post-processed according to steps 1-5 (see Section II) and overlayed with the theoretical data.

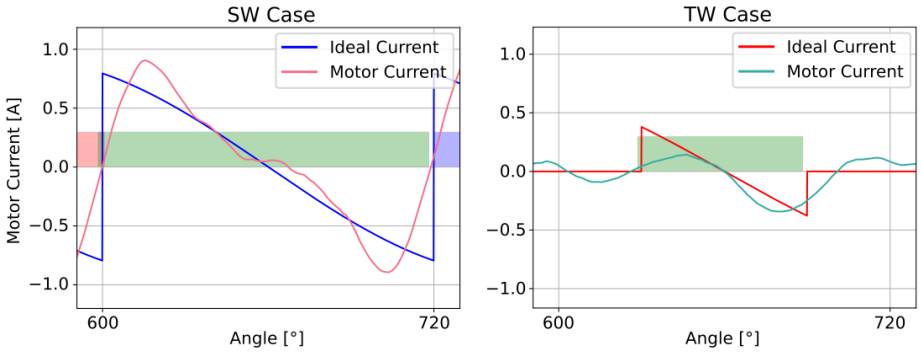

Fig. 6 Exemplary signal fitting results.

For a better visual evaluation of the 120° periodicity in Figs. 6 and 8, the measured data is phase tuned to match the ideal data. To estimate the real ground contacts, the contact intervals in these figures were re-adjusted by the angles φ_q: $\varphi_{\mathrm{real}_q} = \varphi_{\mathrm{ideal}_q} - \varphi_q$. It is evident that, due to the simple character of the applied model, there remain some qualitative and quantitative deviations between the theoretical and post-processed measured data. However, we emphasize

that our goal in using the model is not to precisely predict the real motor currents, but to obtain a rough and simplified approximation of the real-world process to use it for a phase tuning of the measured data, as motivated in Section II C. This goal can be achieved, as shown in Fig. 7, outlining the local phase shifts φ_q, mean values (SW: $\bar{\varphi} = 0.54°$, TW: $\bar{\varphi} = -23.02°$) and standard deviations s_φ (SW: $s_\varphi = 0.91°$, TW: $s_\varphi = 2.42°$) for both gaits:

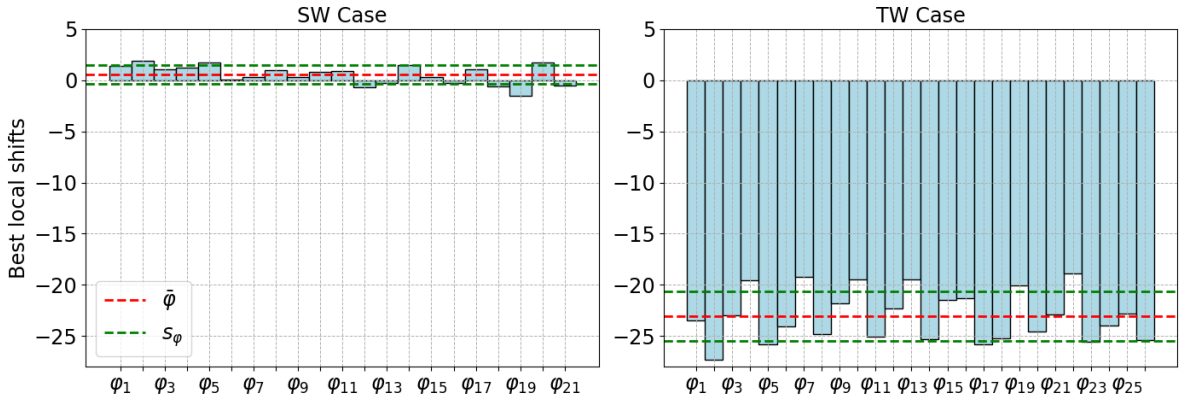

Fig. 7 Evaluation for the best local shifts φ_q in every 120° interval q

Generally, the standard deviations in Fig. 7 might be affected by both the geometric irregularities of the ground and the rimless wheel itself, such as a rotational asymmetry caused by slight variations in leg shape. The first factor can be eliminated due to the controlled testing environment (level ground). However, slight rotational asymmetry resulting from the manufacturing seems likely, as suggested by the 360° periodic pattern observed in Fig. 7 (right). It can be assumed that any significant level of unevenness or a striking obstacle would result both in an increased standard deviation and, locally, in a larger deviation $\varphi_q - \bar{\varphi}$ for the interval q including the obstacle overcoming. Although it was not the primary objective of this work, we also highlight that it is possible to figure out the pre-defined gait type in Section II solely by convolution of the measured motor currents w.r.t. the theoretically generated curves. This serves to validate sufficiency of the theoretical model introduced in Section II B. For a more comprehensive impression of Fig. 6, Fig. 8 shows the motor current signal shifted by the mean angle $\bar{\varphi}$ for the FW-, SW-, and TW case for five exemplary rimless wheel revolutions.

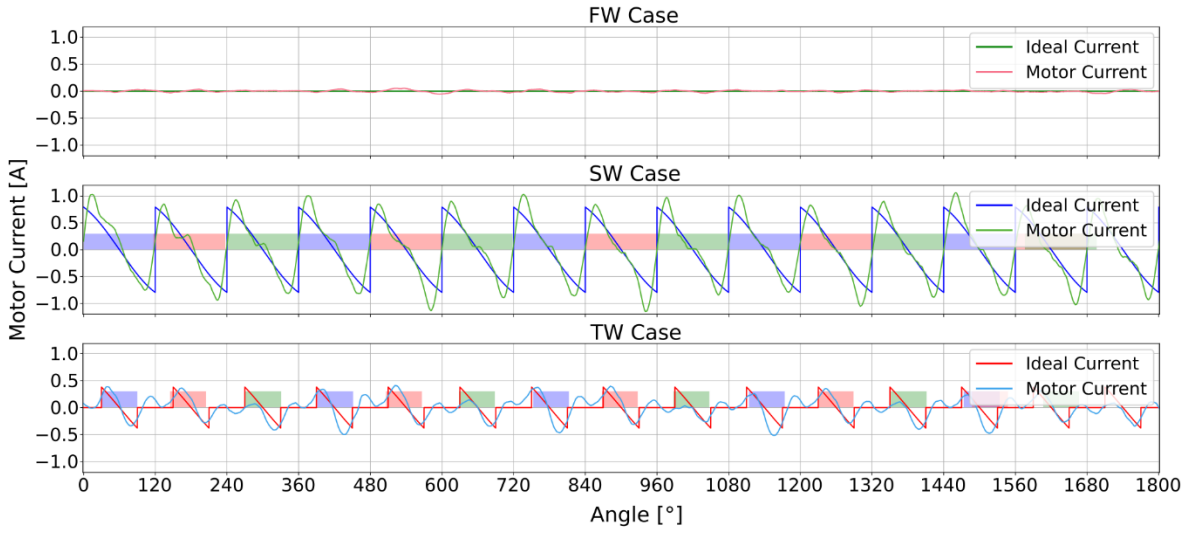

Fig. 8 Ideal / real currents and contacts for FW-, SW-, TW- cases on 5 wheel revolutions

IV. Conclusion and Outlook

This paper presents a novel approach for estimating contact angles between the SCOUT rover's rimless wheels and the ground, based solely on motor current data. The experimental results demonstrate that it is possible to extract meaningful contact information from noisy motor signals without any additional sensors. The proposed algorithm can support different gaits, including synchronous and tripod wheel configurations, which play a significant role in adapting to the unpredictable terrain of lava tubes on Mars and the Moon – the main mission environment.

Future work should focus on recording comprehensive data supported by additional sensors and synchronized video recordings, with the aim of comparing the actual contacts with the estimated ones in order to validate the presented approach. Further investigations should include a proof of concept of the presented approach in highly irregular environments and when overcoming striking obstacles. Additionally, extending the algorithm to adapt to a wider range of gaits and speeds will be valuable for ensuring robust performance across diverse planetary landscapes.

Acknowledgements: We sincerely thank Dr. Sylvia Bräunig for her kind support.

REFERENCES:

[1] NASA. (2020). *Mars Exploration Rovers: Spirit and Opportunity*. NASA Science. Retrieved October 9, 2024, from https://science.nasa.gov/mission/mars-exploration-rovers-spirit-and-opportunity/

[2] Andersson, N. (2023). Developing High level Behaviours for the Boston Dynamics Spot Using Automated Planning. *Developing High level Behaviours for the Boston Dynamics Spot Using Automated Planning*.

[3] Garcia, J. (2018). Boston Dynamics' Atlas robot now performs parkour. *UWIRE Text*, 1–1.

[4] Bruzzone, L., & Quaglia, G. (2012). Locomotion systems for ground mobile robots in unstructured environments. *Mechanical sciences, 3*, 49–62.

[5] Dunker, P. A., Lewinger, W. A., Hunt, A. J., & Quinn, R. D. (2009). A biologically inspired robot for lunar in-situ resource utilization. *2009 IEEE/RSJ International Conference on Intelligent Robots and Systems*, (S. 5039–5044).

[6] Altendorfer, R., Moore, N., Komsuoglu, H., Buehler, M., Brown, H. B., McMordie, D., . . . Koditschek, D. E. (2001). Rhex: A biologically inspired hexapod runner. *Autonomous Robots, 11*, 207–213.

[7] Sonsalla, R. U., Akpo, J. B., & Kirchner, F. (2015). Coyote iii: Development of a modular and highly mobile micro rover. *Proc. of the 13th Symp. on Advanced Space Technologies in Robotics and Automation (ASTRA-2015).*

[8] Boxerbaum, A. S., Oro, J., Peterson, G., & Quinn, R. D. (2008). The latest generation Whegs™ robot features a passive-compliant body joint. *2008 IEEE/RSJ International Conference on Intelligent Robots and Systems*, (S. 1636–1641).

[9] Sanchez, E. S. (2018). *Rowdy runner II: an independently actuated rimless wheel robot.* Master's thesis, The University of Texas at San Antonio.

[10] Schlee, D., Vyas, S., Domınguez, R., & Kirchner, F. (2024). Gait Analysis and Control of Rimless Wheel Rovers for Planetary Exploration.

[11] Stubbig, L., Lichtenheldt, R., Becker, F., & Zimmermann, K. (2017). Model-based development of a compliant locomotion system for a small scout rover. *Ilmenau Scientific Colloquium 59 (www. db-thueringen. de)*, *59*.

[12] Kim, D., & Möller, R. (2006). Passive sensing and active sensing of a biomimetic whisker. *International Conference on the Simulation and Synthesis of Living Systems. Bloomington: Indiana University Press*, (S. 127–131).

[13] Solomon, J. H., & Hartmann, M. J. (2010). Extracting object contours with the sweep of a robotic whisker using torque information. *The International Journal of Robotics Research 29(9)*, (S. 1233-1245).

[14] Merker, L., Steigenberger, J., Marangoni, R., & Behn, C. (2021). A vibrissa-inspired highly flexible tactile sensor: scanning 3d object surfaces providing tactile images. *Sensors, 21*, 1572.

[15] Skibbe, J. (2021). Analysis of phase shifts for a rimless wheel rover. *2021 IEEE Aerospace Conference (50100)*, (S.1–7).

[16] Iwatani, Y., & Takei, T. (2022). Steady locomotion in torso-actuated rimless wheel robots. *SICE Journal of Control, Measurement, and System Integration, 15*, 99–108.